

Symmetry-enforced nodal cage phonons in Th_2BC_2 Meng Wang,¹ Yu Wang,¹ Zhiyong Yang,¹ Jing Fan¹,² Baobing Zheng^{1,3,4,*}, Rui Wang^{1,3,4,5} and Xiaozhi Wu^{3,4,5,†}¹College of Physics and Optoelectronic Technology, Baoji University of Arts and Sciences, Baoji 721016, People's Republic of China²Center for Computational Science and Engineering,

Southern University of Science and Technology, Shenzhen 518055, People's Republic of China

³Institute for Structure and Function & Department of Physics, Chongqing University, Chongqing 400044, People's Republic of China⁴Chongqing Key Laboratory for Strongly Coupled Physics, Chongqing University, Chongqing 400044, People's Republic of China⁵Center of Quantum Materials and Devices, Chongqing University, Chongqing 400044, People's Republic of China

(Received 18 March 2022; revised 12 May 2022; accepted 16 May 2022; published 31 May 2022)

Exploring unique topological states in condensed-matter systems has attracted great interest especially for the topological phonons recently. Based on the unbiased structure prediction approach combined with first-principles calculations, the long-sought crystal structure of Th_2BC_2 is determined. Most importantly, we show by the symmetry analysis and the phonon tight-binding Hamiltonian that Th_2BC_2 hosts nodal surface phonons on the $q_z = \pm\pi$ plane, coexisting with nodal line phonons on the $q_y = 0$ and $q_y = \pm\pi$ planes, consequently, forming cagelike phonons. The nodal surface phonons are protected by the screw axis \tilde{C}_{2z} , and the nodal line phonons are enforced by inversion and time-reversal symmetries, demonstrated by the codimension argument and the effective model analysis. In addition, we also investigate the phonon surface states and the isofrequency arc on the (100) surface, which benefit the confirmation of the nodal cage phonons in experiments. Our paper not only determines the long-sought crystal structure of Th_2BC_2 , but also provides an ideal candidate to realize the exotic topological phonon excitations.

DOI: [10.1103/PhysRevB.105.174309](https://doi.org/10.1103/PhysRevB.105.174309)

I. INTRODUCTION

Following the experimental discovery of quantum Hall effect [1], the studies of topological states become an intense field in condensed-matter physics [2–5]. The typical examples are topological insulators and semimetals, which possess topologically protected surface or edge states that are in favor of topological quantum computation and next-generation low-power electronic devices, thus, attracting considerable attention. In addition to the topological states in the fermionic systems, substantial efforts have been paid to study the analogies in bosonic systems, such as acoustic waves in phononic crystals [6,7], electromagnetic waves in photonics [8,9] and phonons in solids [10–13]. Especially, phonons in solids, which are closely related to the thermal transport, electron-phonon coupling, and thermoelectric effect, provide fertile ground for studying the unconventional topological quasiparticles beyond Dirac and Weyl quasiparticles. Moreover, phonons have unique advantages in contrast to electronic systems because they not only can be explored in the whole frequency range without considering the Fermi level, but also lack the spin-orbital coupling (SOC) so as to realize robust topological quasiparticles against SOC. As a result, various topological phonons are identified very recently, such as the conventional Weyl phonons [10,13–16], Dirac phonons [17,18], the unconventional nodal line

phonons [11,19–22], double-Weyl phonons [10,12,23], hour-glass phonons [13,24], and nodal surface phonons [25–27].

As is well known, the crystalline symmetries play an essential role in protection of topological states. The nodal line quasiparticles, characterized by a quantized Berry phase with a closed path that encircles the nodal line, are generally enforced by additional crystalline symmetries, such as mirror or inversion symmetry combined with time-reversal symmetry [28]. In addition, the nonsymmorphic crystalline symmetries have higher-dimensional projective representations at a certain \mathbf{k} point [29] and, thus, can bring extra degeneracies, then leading to band sticking together at the Brillouin-zone (BZ) boundary. Especially, the nodal surface quasiparticles, whose nodes form a plane in the BZ, are dictated by the existence of nonsymmorphic crystalline symmetries, such as screw rotation symmetry [25,30]. Therefore, the coexistence of the topological nodal line and nodal surface require multiple symmetries, including not only the symmorphic symmetry, i.e., inversion or mirror symmetries, but also the nonsymmorphic screw symmetry. As a result, the coexistence of a nodal line and nodal surface quasiparticles possesses rich interplay between symmetry and topology, but there are a few studies referred to these exotic topological states [27].

In this paper, we uncover that the nodal line and nodal surface phonons can coexist in one of the thorium borocarbide compounds Th_2BC_2 , which may serve as potential nuclear fuel in generation-IV reactors or fission control material and draw renewed attention recently [31,32]. Th_2BC_2 had been prepared by Toth *et al.* [33] for a long time ago. However, its crystal structure has not been determined up to now. On

*scu_zheng@163.com

†xiaozhiwu@cqu.edu.cn

one hand, the complex distributions of B and C atoms in the borocarbides for a given stoichiometry, referred to as the coloring problem, lead to their diversified structural arrangement. On the other hand, owing to the similar electronic and nuclear-scattering cross sections [34], the exact Wyckoff positions of B and C atoms for borocarbides are hard to be identified in experiments. As a result, the crystal structure of Th_2BC_2 remains a long-standing unanswered question. Combining the unbiased structure prediction method and first-principles calculations, we uncover the long-sought crystal structure of Th_2BC_2 . The phonon dispersion and elastic constants of Th_2BC_2 are calculated to demonstrate its structure stability. More importantly, we find that Th_2BC_2 hosts intriguing and unique topological nodal cage phonons consisting of the nodal surface and nodal line phonons. The Berry phase and topological surface states are calculated to confirm its nontrivial properties.

II. COMPUTATIONAL METHODS

Here, the structure prediction employed the particle swarm optimization (PSO) technique as implemented in the CALYPSO code [35,36]. The structure optimizations were carried out in the Vienna *ab initio* simulation package [37] within the framework of density functional theory [38,39]. The Perdew-Burke-Ernzerhof functional [40] and the projector augmented-wave pseudopotentials [41] were chosen to describe the exchange-correlation interaction and the ions-electrons interactions, respectively. The cutoff energy for the plane wave was set to 520 eV, and the BZ was sampled with a Γ -centered Monkhorst-Pack k -point grid [42]. The phonon spectrum of Th_2BC_2 was calculated with the supercell of $2 \times 2 \times 2$ by using the finite displacement method as implemented in PHONOPY [43]. Moreover, the convergence of the phonon spectrum was tested with a larger supercell of $3 \times 3 \times 3$. The topological properties were calculated by the WANNIERTOOLS package [44]. In addition, we also checked the influence of the on-site Coulomb interaction U on the topological phonons by applying the an effective U in a range from 2 to 7 eV. The calculated results show that the topological nodal cage phonons are robust, and only the positions of the band crossings move slightly.

III. RESULTS AND DISCUSSION

To obtain the most energetically stable structure, we perform a comprehensive structure prediction of Th_2BC_2 with the cell up to 8 formula units. Here, to verify the validity and reliability of our prediction, we also carry out the structure prediction of ThBC , ThB_2C , ThBC_2 whose structures had already been determined [45–47]. It is found that the most energetically stable structures of ThBC , ThB_2C , and ThBC_2 are readily reproduced, suggesting the efficiency and reliability of our approach for determining the structures of thorium borocarbide compounds. The most stable predicted structure of Th_2BC_2 crystallizes in an orthorhombic lattice with space-group $Cmcm$ (No. 63) as shown in Fig. 1(a). The fully relaxed lattice constants are $a = 3.712$, $b = 12.823$, and $c = 7.206$ Å. Th atoms occupy the $4a$ Wyckoff position $(0, 0, 0)$ and $4c$ Wyckoff position $(0, 0.7366, 1/4)$, B and C atoms occupy $4c$

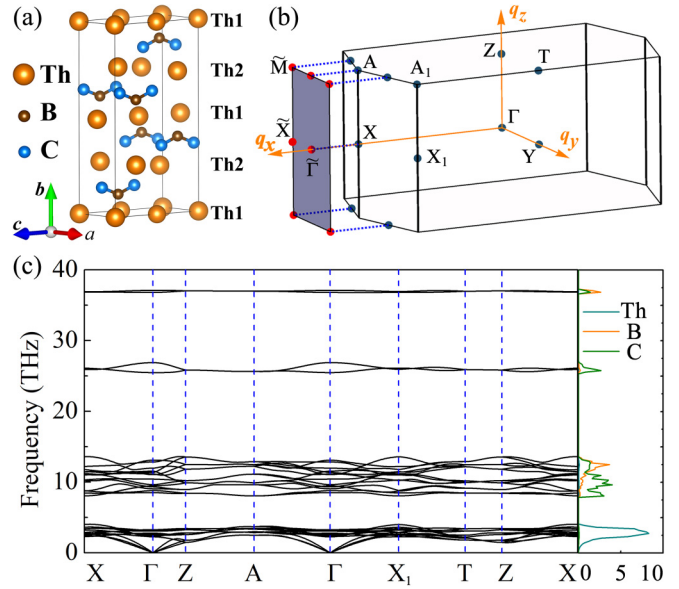


FIG. 1. (a) Crystal structure of Th_2BC_2 , in which the orange, brown, and blue spheres represent the Th, B, and C atoms, respectively. (b) The bulk and (100) surface BZ of Th_2BC_2 where the high-symmetry points in the bulk BZ are marked with dark blue dots, and the high-symmetry points of the surface BZ are denoted by the red dots. (c) Phonon dispersion curves along high-symmetry paths and density of states of Th_2BC_2 .

Wyckoff position $(0, 0.3975, 1/4)$, and $8f$ Wyckoff position $(0, 0.3567, 0.4448)$, respectively.

To evaluate its mechanical stability, we calculate the nine independent elastic constants of Th_2BC_2 . The obtained results are $C_{11} = 190$, $C_{12} = 87$, $C_{13} = 67$, $C_{22} = 173$, $C_{23} = 109$, $C_{33} = 260$, $C_{44} = 80$, $C_{55} = 43$, and $C_{66} = 76$ GPa, which satisfy the elastic stability criteria of orthorhombic crystals ($C_{11} > 0$, $C_{44} > 0$, $C_{55} > 0$, $C_{66} > 0$, $C_{11}C_{22} > C_{12}^2$, $C_{11}C_{22}C_{33} + 2C_{12}C_{13}C_{23} - C_{11}C_{23}^2 - C_{22}C_{13}^2 - C_{33}C_{12}^2 > 0$ [48]), indicating its mechanical stability. The formation energy ΔE_f of Th_2BC_2 is determined with respect to the reference phases of face-centered-cubic thorium, rhombohedral α -boron and graphite, that is, $\Delta E_f = E(\text{Th}_2\text{BC}_2) - 2E(\text{Th}) - E(\text{B}) - 2E(\text{C})$ in which $E(\text{Th}_2\text{BC}_2)$, $E(\text{Th})$, $E(\text{B})$, and $E(\text{C})$ represent the total energies of Th_2BC_2 , face-centered-cubic thorium, rhombohedral α -boron and graphite, respectively. The calculated formation energy ΔE_f of Th_2BC_2 is -1.60 eV, further confirming its feasible preparation in experiment. Moreover, we also calculate the phonon band structure of Th_2BC_2 to verify its thermodynamical stability as shown in Fig. 1(c). Clearly, no imaginary frequency is found in the BZ, indicating the thermodynamical stability of Th_2BC_2 . Considering the mechanical and thermodynamical stabilities and the great success of the powerful PSO technique, we can confirm that the crystal structure of Th_2BC_2 is determined despite lack of further experimental data for comparison.

Owing to the large mass difference of Th, B, and C atoms, the acoustic and optical branches of phonon dispersion of Th_2BC_2 distribute over four different frequency ranges, exhibiting three distinct phonon band gaps. From the phonon

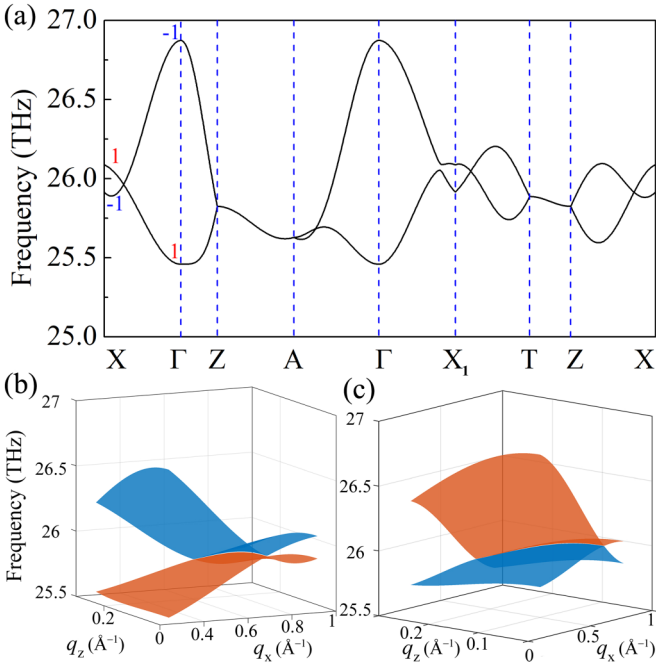


FIG. 2. (a) The enlarged phonon band structure in the frequency range from 25 to 27 THz in which the two crossed bands are denoted by the eigenvalues of \tilde{M}_y . The three-dimensional (3D) representations of phonon dispersions for the optical branches 27 and 28 on the (b) $q_y = 0$ and (c) $q_y = \pm\pi$ planes.

density of states in Fig. 1(c), we find that the low-frequency acoustic and optical modes are dominated by the vibration of Th atoms, whereas the optical branches in the frequency window between 7 and 15 THz originate from the contributions of B and C atoms. Moreover, these phonon bands below 15 THz overlap severely so that they are not clearly identified. However, there are two well-separated optical branches (phonon branches 27 and 28) in a frequency range from 25 to 27 THz, which are mainly attributed to the vibrational modes of C atoms. Therefore, we will mainly focus on these two optical branches from 25 to 27 THz for further study.

The enlarged phonon dispersion between 25 and 27 THz is shown in Fig. 2(a). Along the high-symmetry Z - A and T - Z directions, these two optical branches are stuck together. Besides, the two phonon bands cross linearly along the X - Γ , A - Γ , X_1 - T , and Z - X directions. The high-symmetry X - Γ , A - Γ , and Z - X lines lie on the $q_y = 0$ plane, whose little group contains the identity operator E and glide plane of $\tilde{M}_y = \{M_y|0, 0, 1/2\}$, i.e., $\{E, \tilde{M}_y\}$. Therefore, the two touching bands belong to different irreducible representations so that we can mark the two bands with the eigenvalues ± 1 of \tilde{M}_y as labeled in Fig. 2(a). In addition, the 3D representation of phonon dispersion on the $q_y = 0$ plane is shown in Fig. 2(b). It is found that any high-symmetry lines that connected the arbitrary point along Γ - Z and the arbitrary point along X - A host doubly degenerate points. For the plane of $q_y = \pm\pi$, the little group is the same as the case on the $q_y = 0$ plane, so there exist the similar band crossings on the $q_y = \pm\pi$ plane, which can be marked with the eigenvalues ± 1 of \tilde{M}_y . Meanwhile, we plot the 3D representation of phonon dispersion on the $q_y = \pm\pi$ plane as depicted in Fig. 2(c). Clearly, it can be seen

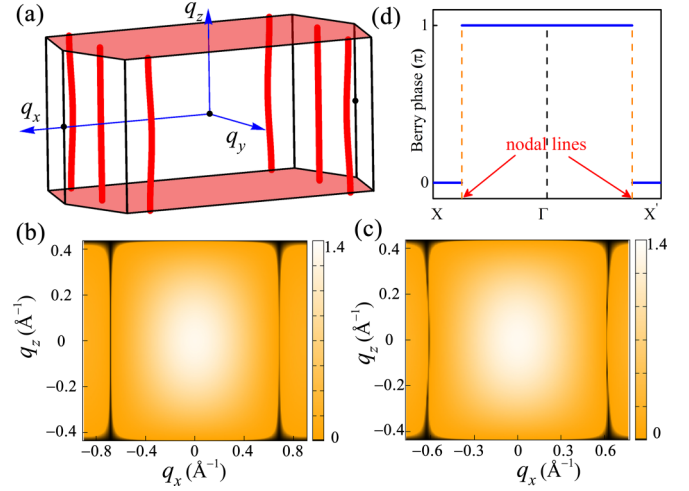


FIG. 3. (a) The nodal cage phonons between the optical branches 27 and 28 in the bulk BZ, which consist of nodal surface phonons on the $q_z = \pm\pi$ plane and the nodal line phonons on the $q_y = 0$ and $q_y = \pm\pi$ planes. The red lines and surfaces, respectively, denote the nodal-line and nodal-surface phonons. The frequency difference maps between these two optical branches in the (b) $q_y = 0$ and (c) $q_y = \pm\pi$ planes. (d) The evolution of the Berry phase for a closed loop \mathcal{L} that encircles the nodal line phonons.

that the band crossings emerge along the high-symmetry paths terminated by arbitrarily selected points on X_1 - A_1 and on Y - T .

To obtain all the doubly degenerate nodal points between these two optical branches and investigate their topological properties, we construct a phonon tight-binding Hamiltonian based on the dynamical matrix $D(\mathbf{q})$ of Th_2BC_2 , which can be built by the force constants tensors between atom i in unit-cell l and atom j in unit-cell l' ,

$$\Phi_{\alpha\beta} \begin{pmatrix} l & l' \\ i & j \end{pmatrix} = \frac{\partial^2 U}{\partial u_{\alpha}(i) \partial u_{\beta}(j)}. \quad (1)$$

α and β are Cartesian indices, and $u_{\alpha}(i)$ denotes the displacement of the i th atom in the l th unit cell away from the equilibrium position. Here, the force constants are treated as the tight-binding parameters. Based on the phonon tight-binding Hamiltonian, the nodal points between phonon branches 27 and 28 in the whole BZ can be obtained as depicted in Fig. 3(a). It can be found that all the k points on the whole $q_z = \pm\pi$ plane are doubly degenerate, forming a plane completely composed of twofold-degenerate nodal points, referred to as nodal surface phonons [25,26]. In addition, we can clearly see the nodal lines that symmetrically lie in the $q_y = 0$ and $q_y = \pm\pi$ planes. All the doubly degenerate nodal points between optical branches 27 and 28 form a cagelike pattern with closed bottom and top in the BZ, so we call it nodal cage phonons. Note that the nodal cage explored here is another type of nodal cage phonons, which are completely different with the nodal cage phonons composed of the neck points of hourglass dispersion proposed in our previous work [24]. To gain a deeper insight into the nodal cage phonons, the frequency differences between the optical branches 27 and 28 are calculated as shown in Fig. 3(b) for the $q_y = 0$ and Fig. 3(c) for the $q_y = \pm\pi$ planes, respectively. The obtained results

show excellent consistency with the nodal point calculation, further exhibiting the shape of the nodal cage phonons.

Next, we provide a symmetry analysis to gain a deeper insight into the nodal cage phonons. Th_2BC_2 belongs to the space-group $Cmcm$, which contains screw axis $\tilde{C}_{2z}: (x, y, z) \rightarrow (-x, -y, z + \frac{1}{2})$, glide plane $\tilde{M}_y: (x, y, z) \rightarrow (x, -y, z + \frac{1}{2})$, spatial inversion \mathcal{I} symmetry. In addition, the time-reversal \mathcal{T} symmetry is preserved for the spinless phononic system. As a result, the high-symmetry $q_z = \pm\pi$ plane is the invariant subspace of the product of \mathcal{T} and \tilde{C}_{2z} . Therefore, we can choose each Bloch state $|u\rangle$ on this plane as an eigenstate of $\mathcal{T}\tilde{C}_{2z}$, and one can easily find

$$(\mathcal{T}\tilde{C}_{2z})^2 = e^{-iq_z} = -1. \quad (2)$$

The antiunitary symmetry $(\mathcal{T}\tilde{C}_{2z})^2 = -1$ for the $q_z = \pm\pi$ plane gives rise to Kramers-like degeneracy for these two phonon branches and leads to arbitrary points on the $q_z = \pm\pi$ plane sticking together, consequently, forming the nodal surface.

To demonstrate the nodal line phonons on the $q_y = 0$ and $q_y = \pm\pi$ planes, we employ a two-band $\mathbf{k} \cdot \mathbf{p}$ effective Hamiltonian,

$$H(\mathbf{q}) = \sum_{i=0}^3 d_i(\mathbf{q})\sigma_i, \quad (3)$$

where σ_0 is identity matrix, σ_i ($i = 1-3$) are the three Pauli matrices, $d_i(\mathbf{q})$ are coefficients relevant to phonon wave vectors $\mathbf{q} = (q_x, q_y, q_z)$. Here, the kinetic term $d_0(\mathbf{q})\sigma_0$ is irrelevant to the phonon band touching, so we neglect it in the following discussion. For the spinless phonon of Th_2BC_2 , the \mathcal{I} and \mathcal{T} symmetries are preserved, which guarantee the two-band Hamiltonian to be real valued [49,50]. As a result, the codimension of such a band degeneracy is 2, which is one less than the number of independent variables (q_x, q_y, q_z). Therefore, the nodal points can trace out one-dimensional manifolds in the BZ.

Under the \mathcal{I} and \mathcal{T} symmetries, the $\mathbf{k} \cdot \mathbf{p}$ Hamiltonian is constrained as

$$\mathcal{I}H(\mathbf{q})\mathcal{I}^{-1} = H(\mathcal{I}\mathbf{q}), \quad \mathcal{T}H(\mathbf{q})\mathcal{T}^{-1} = H(\mathcal{T}\mathbf{q}). \quad (4)$$

We can choose $\mathcal{I} = \sigma_3$ and $\mathcal{T} = \mathcal{K}$. Then, Eq. (4) can be simplified into

$$d_1(\mathbf{q}) = 0, \quad d_2(\mathbf{q}) = -d_2(-\mathbf{q}), \quad d_3(\mathbf{q}) = d_3(-\mathbf{q}). \quad (5)$$

On the $q_y = 0$ plane, the nonsymmorphic glide plane \tilde{M}_y constrains the Hamiltonian as

$$\tilde{M}_y H(\mathbf{q}) \tilde{M}_y^{-1} = H(\tilde{M}_y \mathbf{q}), \quad (6)$$

which can be translated into

$$d_2(q_x, q_y = 0, q_z) = 0. \quad (7)$$

Combined with Eqs. (5) and (7), the only left symmetry-constrained condition of the Hamiltonian for the $q_y = 0$ plane is that $d_3(\mathbf{q})$ is an even function with respect to phonon wave vector \mathbf{q} . Subsequently, we expand $d_3(\mathbf{q})$ with the lower orders up to quadratic terms and obtain

$$d_3(q_x, q_y = 0, q_z) = Aq_x^2 + Bq_z^2 + Cq_xq_z + D. \quad (8)$$

Based on above analysis, the frequency of phonon dispersion on the $q_y = 0$ plane can be represented

$$\omega(\mathbf{q}) = \pm \sqrt{[d_3(q_x, q_y = 0, q_z)]^2}. \quad (9)$$

Therefore, the phonon band touching occurs as $d_3(q_x, q_y = 0, q_z) = 0$ on this plane. Clearly, $d_3(q_x, q_y = 0, q_z) = 0$ corresponds to the equation of a hyperbola centered at the Γ point with the conjugate axis of q_z if the conditions of $A > 0$, $B < 0$, $C = 0$, and $D < 0$ are satisfied, consequently, resulting in hyperboliclike nodal lines on the $q_y = 0$ plane. The nodal lines on the $q_y = \pm\pi$ plane can be also understood according to above discussions owing to the preservation of \tilde{M}_y on the $q_y = \pm\pi$ plane. There are two things that we need to pay attention to. The nodal lines for Th_2BC_2 are topologically protected by the combination of \mathcal{I} and \mathcal{T} symmetries, and the \tilde{M}_y symmetry only guarantees that the nodal lines lie on the $q_y = 0$ and $q_y = \pm\pi$ planes. In addition, the high-order terms of $d_3(q_x, q_y = 0, q_z)$ are essential for determining the detailed shape of the hyperboliclike nodal lines. The topological nodal line can be characterized with a quantized Berry phase around a closed path, we next study the Berry phase of the nodal lines to confirm their topological feature. The phonon Berry phase γ around a closed loop L can be defined as

$$\gamma = \oint_L A(\mathbf{q}) \cdot d\mathbf{q}, \quad (10)$$

in which $A(\mathbf{q}) = i \sum_m \langle \varphi_m(\mathbf{q}) | \nabla_{\mathbf{q}} | \varphi_m(\mathbf{q}) \rangle$ is phonon Berry connection. $\varphi_m(\mathbf{q})$ is the phonon Bloch wave function, defined as [51,52]

$$\varphi_m(\mathbf{q}) = \begin{pmatrix} D(\mathbf{q})^{1/2} \mathbf{u}_{\mathbf{q}} \\ \dot{\mathbf{u}}_{\mathbf{q}} \end{pmatrix}, \quad (11)$$

where $\mathbf{u}_{\mathbf{q}}$ and $\dot{\mathbf{u}}_{\mathbf{q}}$ are the displacement and its derivative with respect to time. Based on the above definition, we calculate the evolution of Berry phase around a closed loop that moves from X to X' (the mirror point of X with respect to the $q_x = 0$ plane) as shown in Fig. 3(d). It is found that the Berry phase is π as the closed loop encircles the nodal line, and 0 as the closed loop is away from the nodal line, implying its nontrivial feature.

The topologically protected surface states and isofrequency arc states can characterize the nodal cage phonons. Therefore, we employ the surface Green's function method [53] to calculate the local density of states (LDOS) on the (100) surface based on the phonon tight-binding Hamiltonian. As shown in Fig. 4(a), although the frequency window for the surface LDOS is very narrow owing to the covering of bulk states, the surface states on the (100) surface are clearly visible, facilitating its experimental observation. In addition, we plot the isofrequency arc states of the (100) surface at a frequency of $\omega = 26.01$ THz as depicted in Fig. 4(b). It can be found that the arc states mainly distribute near \tilde{X} of the (100) surface BZ. Due to the presence of glide plane \tilde{M}_y , the isofrequency arc is symmetric about the q_y axis.

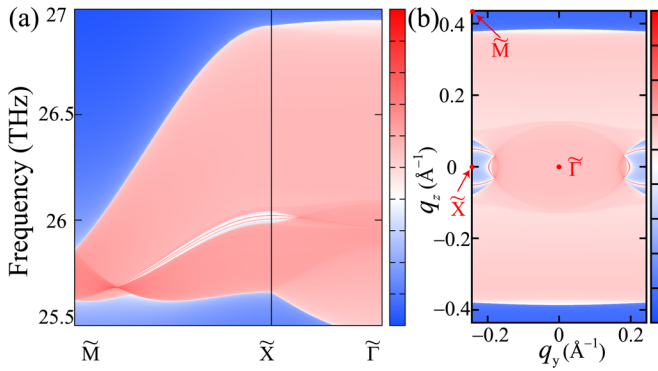


FIG. 4. (a) The LDOs in the frequency range from 25.5 to 27 THz for semi-infinite (100) surface in which \tilde{M} , \tilde{X} , and $\tilde{\Gamma}$ correspond to the high-symmetry point in the surface (100) BZ. (b) The isofrequency arc state of the (100) surfaces at a given frequency of $\omega = 26.01$ THz.

IV. CONCLUSION

To summarize, we determine the long-sought crystal structure of Th_2BC_2 by using the PSO technique within the

framework of first-principles calculations and propose that Th_2BC_2 possesses a nodal surface and nodal line phonons, which form a unique shape, such as a cage with a closed top and bottom, then referred to it as nodal cage phonons. We provide symmetry analysis and a two-band $\mathbf{k} \cdot \mathbf{p}$ effective Hamiltonian to demonstrate the symmetry-protected nodal cage phonons. The results show that the nodal cage phonons are protected by the screw axis \tilde{C}_{2z} , \mathcal{I} , and \mathcal{T} symmetries. Moreover, the calculated surface states and isofrequency arc on the (100) surface confirm their topologically nontrivial feature.

ACKNOWLEDGMENTS

This paper was supported by the National Natural Science Foundation of China (NSFC, Grants No. 11974062, No. 12047564, and No. 11704177), the Natural Science Basic Research Program of Shaanxi (Grant No. 2022JM-001), the Chongqing Natural Science Foundation (Grant No. cstc2019jcyj-msxmX0563), the Fundamental Research Funds for the Central Universities of China (Grants No. 2019CDXYWL0029, and No. 2020CDJQY-A057), and the Center for Computational Science and Engineering of Southern University of Science and Technology.

- [1] K. V. Klitzing, G. Dorda, and M. Pepper, *Phys. Rev. Lett.* **45**, 494 (1980).
- [2] M. Z. Hasan and C. L. Kane, *Rev. Mod. Phys.* **82**, 3045 (2010).
- [3] N. P. Armitage, E. J. Mele, and A. Vishwanath, *Rev. Mod. Phys.* **90**, 015001 (2018).
- [4] T. He, X. Zhang, L. Wang, Y. Liu, X. Dai, L. Wang, and G. Liu, *Mater. Today Phys.* **17**, 100360 (2021).
- [5] W. Meng, X. Zhang, Y. Liu, X. Dai, and G. Liu, *Phys. Rev. B* **104**, 195145 (2021).
- [6] J. Lu, C. Qiu, L. Ye, X. Fan, M. Ke, F. Zhang, and Z. Liu, *Nat. Phys.* **13**, 369 (2017).
- [7] F. Li, X. Huang, J. Lu, J. Ma, and Z. Liu, *Nat. Phys.* **14**, 30 (2018).
- [8] M. Hafezi, S. Mittal, J. Fan, A. Migdall, and J. M. Taylor, *Nat. Photonics* **7**, 1001 (2013).
- [9] M. C. Rechtsman, J. M. Zeuner, Y. Plotnik, Y. Lumer, D. Podolsky, F. Dreisow, S. Nolte, M. Segev, and A. Szameit, *Nature (London)* **496**, 196 (2013).
- [10] T. Zhang, Z. Song, A. Alexandradinata, H. Weng, C. Fang, L. Lu, and Z. Fang, *Phys. Rev. Lett.* **120**, 016401 (2018).
- [11] B. Zheng, B. Xia, R. Wang, Z. Chen, J. Zhao, Y. Zhao, and H. Xu, *Phys. Rev. B* **101**, 100303(R) (2020).
- [12] R. Wang, B. W. Xia, Z. J. Chen, B. B. Zheng, Y. J. Zhao, and H. Xu, *Phys. Rev. Lett.* **124**, 105303 (2020).
- [13] J. Li, J. Liu, S. A. Baronett, M. Liu, L. Wang, R. Li, Y. Chen, D. Li, Q. Zhu, and X.-Q. Chen, *Nat. Commun.* **12**, 1204 (2021).
- [14] Q. Xie, J. Li, S. Ullah, R. Li, L. Wang, D. Li, Y. Li, S. Yunoki, and X.-Q. Chen, *Phys. Rev. B* **99**, 174306 (2019).
- [15] J. Liu, W. Hou, E. Wang, S. Zhang, J.-T. Sun, and S. Meng, *Phys. Rev. B* **100**, 081204(R) (2019).
- [16] B. W. Xia, R. Wang, Z. J. Chen, Y. J. Zhao, and H. Xu, *Phys. Rev. Lett.* **123**, 065501 (2019).
- [17] Z. J. Chen, R. Wang, B. W. Xia, B. B. Zheng, Y. J. Jin, Y.-J. Zhao, and H. Xu, *Phys. Rev. Lett.* **126**, 185301 (2021).
- [18] Y. Jin, R. Wang, and H. Xu, *Nano Lett.* **18**, 7755 (2018).
- [19] J. Li, Q. Xie, J. Liu, R. Li, M. Liu, L. Wang, D. Li, Y. Li, and X.-Q. Chen, *Phys. Rev. B* **101**, 024301 (2020).
- [20] T. T. Zhang, H. Miao, Q. Wang, J. Q. Lin, Y. Cao, G. Fabbris, A. H. Said, X. Liu, H. C. Lei, Z. Fang, H. M. Weng, and M. P. M. Dean, *Phys. Rev. Lett.* **123**, 245302 (2019).
- [21] Q.-B. Liu, H.-H. Fu, G. Xu, R. Yu, and R. Wu, *J. Phys. Chem. Lett.* **10**, 4045 (2019).
- [22] T. Yang, Y. Liu, Z. Wu, X. Wang, and G. Zhang, *Mater. Today Phys.* **18**, 100348 (2021).
- [23] Z. Huang, Z. Chen, B. Zheng, and H. Xu, *npj Comput. Mater.* **6**, 87 (2020).
- [24] B. Zheng, F. Zhan, X. Wu, R. Wang, and J. Fan, *Phys. Rev. B* **104**, L060301 (2021).
- [25] Q.-B. Liu, Z.-Q. Wang, and H.-H. Fu, *Phys. Rev. B* **104**, L041405 (2021).
- [26] C. Xie, H. Yuan, Y. Liu, X. Wang, and G. Zhang, *Phys. Rev. B* **104**, 134303 (2021).
- [27] J. Wang, H. Yuan, Z.-M. Yu, Z. Zhang, and X. Wang, *Phys. Rev. Materials* **5**, 124203 (2021).
- [28] R. Wang, J. Z. Zhao, Y. J. Jin, Y. P. Du, Y. X. Zhao, H. Xu, and S. Y. Tong, *Phys. Rev. B* **97**, 241111(R) (2018).
- [29] S. M. Young and C. L. Kane, *Phys. Rev. Lett.* **115**, 126803 (2015).
- [30] W. Wu, Y. Liu, S. Li, C. Zhong, Z.-M. Yu, X.-L. Sheng, Y. X. Zhao, and S. A. Yang, *Phys. Rev. B* **97**, 115125 (2018).
- [31] P. Rogl, R. Podloucky, H. Noël, and G. Giester, *Acta Mater.* **144**, 484 (2018).
- [32] X.-X. Qu, K. Cao, H. Jiang, Y.-C. Zhao, Z.-H. Dai, Y.-H. Su, and C. Zhang, *J. Phys. Chem. Solids* **122**, 203 (2018).

- [33] L. E. Toth, F. Benesovsky, H. Nowotny, and E. Rudy, *Monatsh. Chem.* **92**, 956 (1961).
- [34] V. Dornich, S. Reynaud, R. A. Haber, and M. Chhowalla, *J. Am. Ceram. Soc.* **94**, 3605 (2011).
- [35] Y. Wang, J. Lv, L. Zhu, and Y. Ma, *Comput. Phys. Commun.* **183**, 2063 (2012).
- [36] Y. Wang, J. Lv, L. Zhu, and Y. Ma, *Phys. Rev. B* **82**, 094116 (2010).
- [37] G. Kresse and J. Furthmüller, *Phys. Rev. B* **54**, 11169 (1996).
- [38] W. Kohn and L. J. Sham, *Phys. Rev.* **140**, A1133 (1965).
- [39] P. Hohenberg and W. Kohn, *Phys. Rev.* **136**, B864 (1964).
- [40] J. P. Perdew, K. Burke, and M. Ernzerhof, *Phys. Rev. Lett.* **77**, 3865 (1996).
- [41] G. Kresse and D. Joubert, *Phys. Rev. B* **59**, 1758 (1999).
- [42] H. J. Monkhorst and J. D. Pack, *Phys. Rev. B* **13**, 5188 (1976).
- [43] A. Togo and I. Tanaka, *Scr. Mater.* **108**, 1 (2015).
- [44] Q. Wu, S. Zhang, H.-F. Song, M. Troyer, and A. A. Soluyanov, *Comput. Phys. Commun.* **224**, 405 (2018).
- [45] P. Rogl, *J. Nucl. Mater.* **79**, 154 (1979).
- [46] P. Rogl and P. Fischer, *J. Solid State Chem.* **78**, 294 (1989).
- [47] X. Zhou and B. Zheng, *Crystals* **9**, 389 (2019).
- [48] F. Mouhat and F.-X. Coudert, *Phys. Rev. B* **90**, 224104 (2014).
- [49] H. Huang, J. Liu, D. Vanderbilt, and W. Duan, *Phys. Rev. B* **93**, 201114(R) (2016).
- [50] A. Tiwari and T. Bzdušek, *Phys. Rev. B* **101**, 195130 (2020).
- [51] Y. Liu, Y. Xu, S.-C. Zhang, and W. Duan, *Phys. Rev. B* **96**, 064106 (2017).
- [52] Y. Liu, Y. Xu, and W. Duan, *Natl. Sci. Rev.* **5**, 314 (2018).
- [53] M. P. L. Sancho, J. M. L. Sancho, J. M. L. Sancho, and J. Rubio, *J. Phys. F: Met. Phys.* **15**, 851 (1985).